

Hermite – Discontinuous Galerkin Overset Grid Methods for the Scalar Wave Equation

Oleksii Beznosov · Daniel Appelö

Received: date / Accepted: date

Abstract We present high order accurate numerical methods for the wave equation that combines efficient Hermite methods with geometrically flexible discontinuous Galerkin methods by using overset grids. Near boundaries we use thin boundary fitted curvilinear grids and in the volume we use Cartesian grids so that the computational complexity of the solvers approach a structured Cartesian Hermite method. Unlike many other overset methods we do not need to add artificial dissipation but we find that the built in dissipation of the Hermite and discontinuous Galerkin methods is sufficient to maintain stability. By numerical experiments we demonstrate the stability, accuracy, efficiency and applicability of the methods to forward and inverse problems.

Keywords Wave equation · Overset grids · High order · Hermite methods · Discontinuous Galerkin methods

Mathematics Subject Classification (2010) MSC 65M60 · MSC 35L05

1 Introduction

Accurate and efficient simulation of waves is important in many areas in science and engineering due to the ability of waves to carry information over large distances. This ability stems from the fact that waves do not change shape in free space. On the other hand when the background medium is changing this induces

Oleksii Beznosov
Department of Mathematics and Statistics,
University of New Mexico,
1 University of New Mexico, MSC01 1115, Albuquerque, NM 87131
E-mail: obeznosov@unm.edu

Daniel Appelö
Department of Applied Mathematics,
University of Colorado,
University of Colorado 526 UCB, Boulder, CO 80309
E-mail: daniel.appelo@colorado.edu

a change in the wave forms that propagate through the medium and the waves can be used for probing the interior material properties of objects.

In order to preserve the properties of waves from the continuous setting it is preferable to use high order accurate discretizations that are able to control dispersive errors. The development of high order methods for wave propagation problems has been an active area of research for a long time and there are by now many attractive methods. Examples include (but are not limited to) finite difference methods, [26, 33, 35, 28, 21], embedded boundary finite differences, [6, 11, 25, 24, 34], element based methods like discontinuous Galerkin (DG) methods, [36, 3, 14, 15, 16, 19], hybridized discontinuous Galerkin (HDG) methods, [27, 29], cut-cell finite elements [31, 30] and Galerkin-difference methods [8].

An advantage of summation-by-parts finite differences and Galerkin type methods is that stability is guaranteed, however this guarantee also comes with some drawbacks. For diagonal norm summation-by-parts finite differences the order of accuracy is reduced to roughly half of that in the interior near boundaries. Further the need for multi-block grids also restricts the geometrical flexibility.

As DG and HDG methods are naturally formulated on unstructured grids they have good geometric flexibility. However, Galerkin based polynomial methods often have the drawback that they require small timesteps (the difference Galerkin and cut-cell finite element methods are less affected by this) when combined with explicit timestepping methods, but on the other hand they preserve high order accuracy all the way up to the boundary and it is easy to implement boundary conditions independent of the order of the method.

The pioneering work by Henshaw and co-authors, see for example [13], describe techniques for generating overset grids as well as how they can be used to solve elliptic and first order time-dependent partial differential equations (PDE) by second order accurate finite differences. In an overset grid method the geometry is discretized by narrow body-fitted curvilinear grids while the volume is discretized on one or more Cartesian grids. The generation of such body-fitted grids is local and typically produces grids of very high quality, [22]. The grids overlap (we say that they are overset) so that the solution on an interior (often referred to as non-physical or ghost) boundary can be transferred from the interior of another grid. In [13] and in most other overset grid methods the transfer of solutions between grids is done by interpolation. Since the bulk of the domain can be discretized on a Cartesian grid the efficiency asymptotically approaches that of a Cartesian solver but still retains the geometrical flexibility of an unstructured grid method. The same type of efficiency can be expected for embedded boundary and cut-cell finite elements but the errors close to physical boundaries are typically smoother and smaller when body-fitted grids are used.

Here we are concerned with the approximation of the scalar wave equation on overset grids. To our knowledge, high order overset grid methods for wave equations in second order form have been restricted to finite difference discretizations. For example, in [23] high order centered finite difference approximations to Maxwell's equations (written as a system of second order wave equations) was introduced. More recently, in [1], the upwind discretizations by Banks and Henshaw introduced in [9] were generalized to overset grids. A second order accurate overset grid method for elastic waves can be found in [2].

We use the recently introduced dissipative Hermite methods for the scalar wave equation in second order form, [5], for the approximation on Cartesian grids. To

handle geometry we use the energy based DG methods of [3] on thin grids that are grown out from physical boundaries. We use projection to transfer the solutions between grids rather than interpolation.

Both the Hermite and DG methods we employ increase the order of accuracy by increasing the number of degrees of freedom on an element or cell. This has practical implications for grid generation as a single grid with minimal overlap can be used independent of order, reducing the complexity of the grid generation step. This can be important for example in problems like optimal shape design, where the boundary changes throughout the optimization. This is different from the finite difference methods where, due to the wider finite difference stencils, the overlap must grow as the order is increased.

The transfer of solutions between overset grids typically causes a perturbation to the discrete operators which, especially for hyperbolic problems, results in instabilities, see [2] for example. These instabilities are often weak and can thus be suppressed by a small amount of artificial dissipation. There are two drawbacks of this added dissipation, first it is often not easy to determine the suitable amount needed, i.e. big enough to suppress instabilities but small enough not to reduce the accuracy or timestep too severely. Second, in certain cases the instabilities are strong enough that the dissipation must scale with the discretization parameter (the grid size) in such a way that the order of accuracy of the overall method is reduced by one.

Similar to [1], we use a dissipative method that has naturally built-in damping that is sufficient to suppress the weak instabilities caused by the overset grids. The order of the hybrid overset grid method is the design order of the Hermite method or DG method, whichever is the smallest.

In the hybrid H-DG overset grid method the Hermite method is used on a Cartesian grid in the interior of the domain, and the discontinuous Galerkin method on another, curvilinear grid at the boundary. The numerical solution is evolved independently on these grids for one timestep of the Hermite method. By using the Hermite method in the interior the strict timestep constraints of the DG method are relaxed by a factor that grows with the order of the method. Asymptotically, as discussed above, the complexity of the hybrid H-DG solver approaches that of the Cartesian Hermite solver [5].

The paper is organized as follows. The Hermite method is described in the next section. We first explain the method in simple one dimensional case and then explain how the method generalizes to two dimensions. The DG method is described in section 3. The details of the overset grids and a hybridization of the DG and the Hermite methods are described in section 4. We illustrate the hybrid H-DG method with numerical simulations in the section 5.

2 Dissipative Hermite method for the scalar wave equation

We present the Hermite method in some detail here and refer the reader to the original work [5] for convergence analysis and error estimates.

Consider the one dimensional wave equation in second order form in space and first order in time

$$u_t = v, \quad (1)$$

$$v_t = c^2 u_{xx} + f, \quad x \in \Omega, \quad t \in (0, T). \quad (2)$$

Here $u \in C^{2m+3}(\Omega \times [0, T])$, $v \in C^{2m+1}(\Omega \times [0, T])$ and $f \in C^{2m+1}(\Omega \times [0, T])$ for optimal convergence. We refer to u as the displacement, and v as the velocity. The speed of sound is c . We consider boundary conditions of Dirichlet or Neumann type

$$u(t, x) = h_0(t, x), \quad x \in \partial\Omega_D,$$

$$u_x(t, x) = h_1(t, x), \quad x \in \partial\Omega_N,$$

and initial conditions

$$u(0, x) = g_0(x),$$

$$v(0, x) = g_1(x).$$

Let the spatial domain be $\Omega = [a, b]$. The domain will be discretized by a primal grid

$$x_i = a + ih, \quad h = (b - a)/N, \quad i = 0, \dots, N,$$

and a dual grid

$$x_i = a + ih, \quad i = \frac{1}{2}, \dots, N - \frac{1}{2}.$$

The use of staggered grids is essential for being able to take large timesteps. In time we discretize using a uniform grid with increments $\Delta t/2$, that is

$$t_n = n\Delta t, \quad n = 0, 1/2, 1, \dots$$

At each grid point x_i the approximation to the solution is represented by its degrees of freedom (DOF) that approximate the values and spatial derivatives of u and v . Equivalently, the approximations to u and v can be represented as polynomials centered at grid points x_i . The Taylor coefficients of these polynomials are scaled versions of the degrees of freedom. To achieve the optimal order of accuracy $(2m + 1)$ we require the $(m + 1)$ and m first derivatives of u and v respectively to be stored at each grid point.

At the initial time (which we take to be $t = 0$) these polynomials are approximations to the initial condition on the primal grid

$$u(x, 0) \approx \sum_{l=0}^{m+1} \hat{u}_l \left(\frac{x - x_i}{h} \right)^l \equiv p_i(x), \quad i = 0, \dots, N,$$

$$v(x, 0) \approx \sum_{l=0}^m \hat{v}_l \left(\frac{x - x_i}{h} \right)^l \equiv q_i(x), \quad i = 0, \dots, N.$$

The coefficients \hat{u}_l and \hat{v}_l are assumed to be accurate approximations to the scaled Taylor coefficients of the initial data. If expressions for the derivatives of the initial data are known we simply set

$$\hat{u}_l = \frac{h^l}{l!} \frac{d^l g_0}{dx^l} \Big|_{x=x_i}, \quad \hat{v}_l = \frac{h^l}{l!} \frac{d^l g_1}{dx^l} \Big|_{x=x_i}. \quad (3)$$

Alternatively, if only the functions g_0 and g_1 are known, we may use a projection or interpolation procedure to find the coefficients in (3).

The numerical algorithm for a single timestep consists of two phases, an interpolation step and an evolution step. First, during the interpolation phase the spatial piecewise polynomials are constructed to approximate the solution at the current time. Then, in the time evolution phase we use the spatial derivatives of the interpolation polynomials to compute time derivatives of the solution using the PDE. We compute new values of the DOF on the next time level by evaluating the obtained Taylor series. We now describe each step separately.

2.1 Hermite interpolation

At the beginning of a timestep at time t_n (or at the initial time) we consider a cell $[x_i, x_{i+1}]$ and construct the unique local Hermite interpolant of degree $(2m + 3)$ for the displacement and degree $(2m + 1)$ for the velocity. The interpolating polynomials are centered at the dual grid points $x_{i+\frac{1}{2}}$ and can be written in Taylor form

$$p_{i+\frac{1}{2}}(x) = \sum_{l=0}^{2m+3} \hat{u}_{l,0} \left(\frac{x - x_{i+\frac{1}{2}}}{h} \right)^l, \quad x \in [x_i, x_{i+1}], \quad i = 0, \dots, N-1, \quad (4)$$

$$q_{i+\frac{1}{2}}(x) = \sum_{l=0}^{2m+1} \hat{v}_{l,0} \left(\frac{x - x_{i+\frac{1}{2}}}{h} \right)^l, \quad x \in [x_i, x_{i+1}], \quad i = 0, \dots, N-1. \quad (5)$$

The interpolants $p_{i+\frac{1}{2}}$ and $q_{i+\frac{1}{2}}$ are determined by the local interpolation conditions:

$$\begin{aligned} \frac{d^l p_{i+\frac{1}{2}}}{dx^l} &= \frac{d^l p_i}{dx^l} \Big|_{x=x_i}, \quad \frac{d^l p_{i+\frac{1}{2}}}{dx^l} = \frac{d^l p_{i+1}}{dx^l} \Big|_{x=x_{i+1}}, \quad l = 0, \dots, m+1, \\ \frac{d^l q_{i+\frac{1}{2}}}{dx^l} &= \frac{d^l q_i}{dx^l} \Big|_{x=x_i}, \quad \frac{d^l q_{i+\frac{1}{2}}}{dx^l} = \frac{d^l q_{i+1}}{dx^l} \Big|_{x=x_{i+1}}, \quad l = 0, \dots, m. \end{aligned}$$

We find the coefficients in (4) and (5) by forming a generalized Newton table as described in [20].

2.2 Time evolution

To evolve the solution in time we further expand the coefficients of $p_{i+\frac{1}{2}}$ and $q_{i+\frac{1}{2}}$. At each point on the dual grid, $x_{i+\frac{1}{2}}$ we seek temporal Taylor series

$$p_{i+\frac{1}{2}}(x, t) = \sum_{l=0}^{2m+3} \sum_{s=0}^{\kappa_p} \hat{u}_{l,s} \left(\frac{x - x_{i+\frac{1}{2}}}{h} \right)^l \left(\frac{t}{\Delta t} \right)^s, \quad (6)$$

$$q_{i+\frac{1}{2}}(x, t) = \sum_{l=0}^{2m+1} \sum_{s=0}^{\kappa_q} \hat{v}_{l,s} \left(\frac{x - x_{i+\frac{1}{2}}}{h} \right)^l \left(\frac{t}{\Delta t} \right)^s, \quad (7)$$

where $\kappa_p = (2m + 3 - 2\lfloor \frac{l}{2} \rfloor)$ and $\kappa_q = (2m + 1 - 2\lfloor \frac{l}{2} \rfloor)$. The coefficients $\hat{u}_{l,0}$ and $\hat{v}_{l,0}$ are given by the coefficients of (4) and (5). At this time the scaled time derivatives, $\hat{u}_{l,s}$ and $\hat{v}_{l,s}$ $s > 0$, are unknown and must be determined. Once they are determined we may simply evaluate (6) and (7) at $t = t_n + \Delta t/2$ to find the solution at the next half timestep.

In Hermite methods the coefficients of temporal Taylor polynomials are determined by collocating the differential equation, [18, 5, 20]. In particular, by differentiating (1) and (2) in space and time the time derivatives of the solution can be directly expressed in terms of spatial derivatives

$$\frac{\partial^{s+1+r} u}{\partial t^{s+1} \partial x^r} = \frac{\partial^{s+r} v}{\partial t^s \partial x^r}, \quad (8)$$

$$\frac{\partial^{s+1+r} v}{\partial t^{s+1} \partial x^r} = c^2 \frac{\partial^{s+r+2} u}{\partial t^s \partial x^{r+2}} \frac{\partial^s u}{\partial t^s \partial x^2} + \frac{\partial^{s+r} f}{\partial t^s \partial x^r}. \quad (9)$$

Substituting (6) and (7) into (8) and (9) and evaluating at $x = x_{i+\frac{1}{2}}$ and $t = t_n$, we can match the powers of the coefficients to find the recursion relations

$$\hat{u}_{l,s+1} = \frac{\Delta t}{s} \hat{v}_{l,s}, \quad (10)$$

$$\hat{v}_{l,s+1} = c^2 \frac{(l+1)(l+2)}{h^2} \frac{\Delta t}{s} \hat{u}_{l+2,s} + \frac{\Delta t}{s} \hat{f}_{l,s}. \quad (11)$$

Here $\hat{f}_{l,s}$ are the coefficients of the Taylor expansion of f , or of the polynomial which interpolates $f(t, x_{i+\frac{1}{2}})$ in time around $t = t_n$. Note that since there are a finite number of coefficients, representing the spatial derivatives at the time t_n , the recursions truncate and only κ_p and κ_q terms need to be considered.

To complete a half timestep we evaluate the approximation at $t = t_n + \frac{\Delta t}{2}$ for the $(m+1)$ and m first derivatives

$$\frac{\partial^l u}{\partial x^l}(x_{i+\frac{1}{2}}, t_{n+\frac{1}{2}}) \approx \frac{\partial^l p_{i+\frac{1}{2}}}{\partial x^l}(x_{i+\frac{1}{2}}, t_{n+\frac{1}{2}}) = \frac{l!}{h^l} \sum_{s=0}^{\kappa_p} \frac{\hat{u}_{l,s}}{2^s}, \quad l = 0, \dots, m+1, \quad (12)$$

$$\frac{\partial^l v}{\partial x^l}(x_{i+\frac{1}{2}}, t_{n+\frac{1}{2}}) \approx \frac{\partial^l q_{i+\frac{1}{2}}}{\partial x^l}(x_{i+\frac{1}{2}}, t_{n+\frac{1}{2}}) = \frac{l!}{h^l} \sum_{s=0}^{\kappa_q} \frac{\hat{v}_{l,s}}{2^s}, \quad l = 0, \dots, m. \quad (13)$$

Abstract Remark 1 For a piecewise polynomial solution to the wave equation all the terms in the Taylor series are present in the right-hand side of equations (12)-(13). A consequence is that the time evolution is exact whenever the forcing is zero (or a polynomial of degree $2m+1$) and each cell $[x_i, x_{i+1}]$ includes the domain of the dependence of the solution at a dual grid point $x_{i+\frac{1}{2}}$ at time $t = \frac{\Delta t}{2}$, that is, when

$$c \frac{\Delta t}{2} \leq \frac{h}{2}.$$

2.3 Imposing boundary conditions

Physical boundary conditions are enforced at the half time level, i.e. when the solution on the dual grid is to be advanced back to the primal grid. As there are many degrees of freedom that are located on the boundary the physical boundary condition must be augmented by the differential equation to generate more

equations so that the degrees of freedom can be uniquely determined. The basic principle, often referred to as compatibility boundary conditions (see e.g. [23]), is to take tangential derivatives of the PDE and the boundary conditions so that a sufficient number of boundary conditions are obtained.

For example, assume we want to impose the boundary condition

$$u(t, 0) = g(t). \quad (14)$$

Then, as $x_0 = 0$ is a boundary grid point the Taylor polynomials (6)-(7) centered at x_0 should satisfy the boundary condition (14). In addition it should also satisfy the differential equation and derivatives of (14). We thus seek a polynomial outside the domain which together with the polynomial just inside the boundary forms a Hermite interpolant that satisfies the boundary and compatibility conditions.

Precisely, to find the polynomial describing u at time t we must determine $2(m+2)$ unknowns that specify the polynomial at the boundary. First, this polynomial must interpolate the $(m+2)$ data describing the current approximation of u at $x_{\frac{1}{2}}$, this yields $(m+2)$ independent linear equations. Second, the first of the remaining $(m+2)$ independent linear equations can be obtained by requiring that the polynomial coincides with the boundary condition $u(0, t) = g(t)$. The next equation is $g_{tt}(t) = u_{tt}(0, t) = u_{xx}(0, t)$, and so forth.

Once the interpolant is determined on the boundary we evolve it as in the interior (see section 2.2).

Remark 2 We note that in the special case of a flat boundary and homogeneous Dirichlet or Neumann boundary conditions then enforcing the boundary conditions reduces to enforcing that the polynomial on the boundary is either odd or even, respectively, in the normal direction. Then the correct odd polynomial can be obtained by constructing the polynomial outside the domain Ω (often referred as ghost-polynomial) by mirroring the coefficients corresponding to even powers in the normal coordinate variable with a negative sign and the coefficients corresponding to odd powers with the same sign.

Boundary conditions at interior overset grid boundaries are supplied by projection of the known solutions from other grids and will be discussed below.

2.4 Higher dimensions

In higher dimensions the approximations to u and v take the form of centered tensor product Taylor polynomials. In two dimensions (plus time) the coefficients would be of the form $c_{k,l,s}$, with the two first indices representing the powers in the two spatial directions, and the third representing time.

For the scalar wave equation

$$\begin{aligned} u_t &= v, \\ v_t &= c^2(u_{xx} + u_{yy}), \quad (x, y) \in \Omega, \quad t > 0, \end{aligned}$$

the recursion relations for computing the time derivatives are a straightforward generalization of the one dimensional case

$$c_{k,l,s} = \frac{\Delta t}{s} d_{k,l,s-1}, \quad (15)$$

$$d_{k,l,s} = c^2 \frac{(k+2)(k+1)}{s} \frac{\Delta t}{h_x^2} c_{k+2,l,s-1} + c^2 \frac{(l+2)(l+1)}{s} \frac{\Delta t}{h_y^2} c_{k,l+2,s-1}. \quad (16)$$

As noted in [5], using this recursion for all the time derivatives does not produce a method with order independent CFL condition but a method whose time-step size decrease slightly as the order increases. For optimally large timesteps it is necessary to use the special start up procedure

$$\begin{aligned} c_{k,l,1} &= \Delta t d_{k,l,0}, \\ d_{k,l,1} &= (c\Delta t)^2 \left(\frac{(k+2)(k+1)}{h_x^2} c_{k+2,l}^X + \frac{(l+2)(l+1)}{h_y^2} c_{k,l+2}^Y \right). \end{aligned}$$

Here $c_{k,l}^X$ are the $(2m+4) \times (2m+2)$ coefficients of the interpolating polynomial of degree $(2m+3)$ in x and degree $(2m+1)$ in y and $c_{k,l}^Y$ are the $(2m+4) \times (2m+2)$ coefficients of the interpolating polynomial of degree $(2m+3)$ in y and degree $(2m+1)$ in x . For the remaining coefficients $s = 2 \dots, 4m+3$ we use (15) and (16) with $k, l = 0, \dots, 2m+1$. Further details of the two dimensional method can be found in [5].

3 Energy based discontinuous Galerkin methods for the wave equation

Our spatial discontinuous Galerkin discretization is a direct application of the energy based formulation described for general second order wave equations in [3, 4, 7]. Here, our energy based DG method starts from the energy of the scalar wave equation

$$H(t) = \int_{\Omega} \frac{v^2}{2} + G(x, y, \nabla u) d\Omega,$$

where $G(x, y, \nabla u) = \frac{c^2(x, y)}{2} |\nabla u|^2$ is the potential energy density, v is the velocity or the time derivative of the displacement, $v = u_t$.

Now, the wave equation, written as a second order equation in space and first order in time takes the form

$$u_t = v, \quad v_t = -\delta G,$$

where δG is the variational derivative of the potential energy

$$\delta G = -\nabla \cdot (c^2(x, y) \nabla u).$$

For the continuous problem the change in energy is

$$\frac{dH(t)}{dt} = \int_{\Omega} v v_t + u_t \left[\nabla \cdot (c^2(x, y) \nabla u) \right] d\Omega = [u_t (n \cdot (c^2(x, y) \nabla u))]_{\partial\Omega},$$

where the last equality follows from integration by parts together with the wave equation.

A variational formulation that mimics the above energy identity can be obtained if the equation $v - u_t = 0$ is tested with the variational derivative of the potential energy. Let Ω_j be an element and $(\Pi^{q_u}(\Omega_j))^2$ and $(\Pi^{q_v}(\Omega_j))^2$ be the spaces of tensor product polynomials of degrees q_u and $q_v = q_u - 1$. Then, the variational formulation on that element is:

Problem 1 Find $v^h \in (\Pi^{q_v}(\Omega_j))^2$, $u^h \in (\Pi^{q_u}(\Omega_j))^2$ such that for all $\psi \in (\Pi^{q_v}(\Omega_j))^2$, $\phi \in (\Pi^{q_u}(\Omega_j))^2$

$$\int_{\Omega_j} (c^2 \nabla \phi) \cdot \left(\frac{\partial \nabla u^h}{\partial t} - \nabla v^h \right) d\Omega = [(c^2 \nabla \phi) \cdot n (v^* - v^h)]_{\partial \Omega_j}, \quad (17)$$

$$\int_{\Omega_j} \psi \frac{\partial v^h}{\partial t} + c^2 \nabla \psi \cdot \nabla u^h d\Omega = [\psi (c^2 \nabla u \cdot n)^*]_{\partial \Omega_j}. \quad (18)$$

Let $[[f]]$ and $\{f\}$ denote the jump and average of a quantity f at the interface between two elements, then, choosing the numerical fluxes as

$$\begin{aligned} v^* &= \{v^h\} - \tau_1 [[c^2 \nabla u^h \cdot n]], \\ (c^2 \nabla u \cdot n)^* &= \{c^2 \nabla u^h \cdot n\} - \tau_2 [[v^h]], \end{aligned}$$

yields a contribution $-\tau_1 ([[c^2 \nabla u^h \cdot n]])^2 - \tau_2 ([[v^h]])^2$ from each element face to the change of the discrete energy, guaranteeing that

$$\frac{dH^h(t)}{dt} \equiv \frac{d}{dt} \sum_j \int_{\Omega_j} \frac{(v^h)^2}{2} + G(x, y, \nabla u^h) \leq 0.$$

Physical boundary conditions are enforced through the numerical fluxes, see [3] for details.

Note that the above energy estimate follows directly from the formulation (17) - (18) but as the energy is invariant to constants equation (17) must be supplemented by the equation

$$\int_{\Omega_j} \left(\frac{\partial u^h}{\partial t} - v^h \right) d\Omega = 0.$$

Our implementation uses quadrilaterals and approximations by tensor product Chebyshev polynomials of the solution on the reference element $(r, s) \in [-1, 1]^2$. That is, on each quadrilateral we have approximations on the form

$$\begin{aligned} u(x(r, s), y(r, s), t_n) &\approx \sum_{l=0}^{q_u} \sum_{k=0}^{q_u} c_{lk} T_l(r) T_k(s), \\ v(x(r, s), y(r, s), t_n) &\approx \sum_{l=0}^{q_v} \sum_{k=0}^{q_v} d_{lk} T_l(r) T_k(s). \end{aligned}$$

We choose $\tau_1 = \tau_2 = 1/2$ (so called upwind or Sommerfeld fluxes) which result in methods where u is observed to be $q_u + 1$ order accurate in space [3].

3.1 Taylor series time-stepping

In order to match the order of accuracy in space and time for the DG method we employ Taylor series time-stepping. Assuming that all the degrees of freedom have been assembled into a vector \mathbf{w} we can write the semi-discrete method as $\mathbf{w}_t = A\mathbf{w}$ with A being the matrix representing the spatial discretization. If we know the discrete solution at the time t_n we can advance it to the next time step $t_{n+1} = t_n + \Delta t$ by the simple formula

$$\begin{aligned}\mathbf{w}(t_n + \Delta t) &= \mathbf{w}(t_n) + \Delta t \mathbf{w}_t(t_n) + \frac{(\Delta t)^2}{2!} \mathbf{w}_{tt}(t_n) \dots \\ &= \mathbf{w}(t_n) + \Delta t A \mathbf{w}(t_n) + \frac{(\Delta t)^2}{2!} A^2 \mathbf{w}(t_n) \dots\end{aligned}$$

As we use dissipative fluxes this timestepping method is stable as long as the number of stages in the Taylor series is greater than the order of accuracy in space and with the timestep small enough.

4 Overset grid methods

In this section we explain how we use the two discretization techniques described above on overset grids to approximate solutions to the scalar wave equation.

The idea behind the overset grid methods is to cover the bulk of the domain with a Cartesian grid, where efficient methods can be employed, and to discretize the geometry with narrow body-fitted grids. In Figure 1 we display two overset grids, a blue Cartesian grid, which we denote a , and a red curvilinear grid, which we denote b , that are used to discretize a geometry consisting of a circular hole cut out from a square region. Note that the grids overlap, hence the name overset grids. Also, note that the annular grid cuts out a part of the Cartesian grid. This cut of the Cartesian grid creates an internal, non-physical boundary in the blue grid.

Here physical boundary conditions are enforced on the red grid at the black boundary which defines the inner circle and on the outermost boundary on the blue grid.

In order to use the Hermite or DG methods on the grids we will need to supply boundary conditions at the interior boundaries. In the example in Figure 1 this means that we would have to specify the solution on the outer part of the annular grid and on the staircase boundary (marked with filled black circles) that has been cut out from the Cartesian grid.

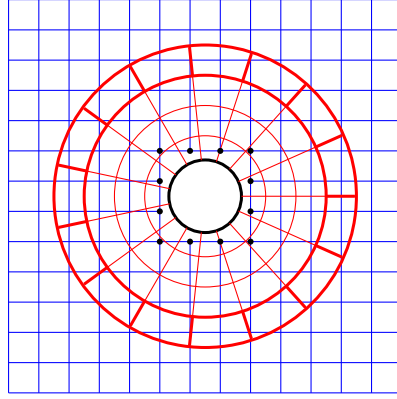


Fig. 1 An example of an overset grid for a circular boundary inside a square. The red grid is curvilinear and the blue grid is Cartesian (in a realistic problem the red grid would be significantly thinner). The black filled circles indicate the cut out domain boundary.

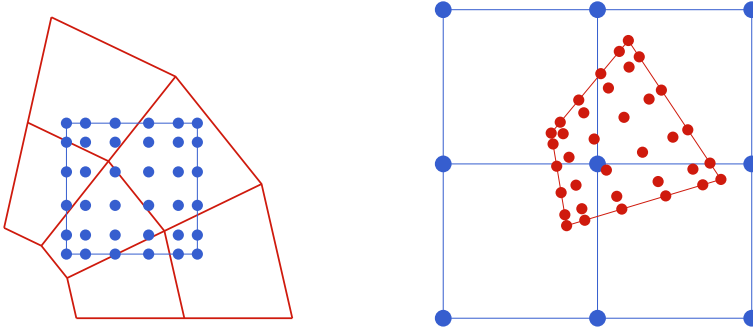


Fig. 2 Typical setup for communication. In the left subfigure the local tensor product GLL grid around a Hermite grid point is marked with filled blue circles. The points in the GLL grid may be covered by different DG elements. In the right subfigure the tensor product grid inside the DG element is marked with filled red circles. The points in the GLL grid may be contained in different Hermite cells.

In most methods that use overset grids, in particular those using finite differences, the communication of the solution on the interior boundaries is done by interpolation, see e.g. [13]. For the methods we use here we have found that the stability properties are greatly enhanced if we instead transfer volumetric data (numerical solution) in the elements / gridpoints near the internal boundaries by projection rather than by interpolation. In fact, when we use volume data the resulting methods are stable without adding artificial dissipation, when we use interpolation they are not.

As mentioned above, in a Hermite method, we can think of the degrees of freedom as either being nodal data, consisting of function and derivative values, or as coefficients in a Taylor polynomial. Thus, when transferring data to a grid where a Hermite method is used (like the example in the left subfigure of Figure 1) we must determine a tensor product polynomial centered around a gridpoint

local to that grid (the points we would center around are indicated by black points in Figure 1). Below we will explain in detail how we determine this polynomial.

For elements with an internal boundary face (denoted by thick red lines in Figure 1) we could in principle transfer the solution by specifying a numerical flux on that face, however we have found that this approach results in weakly unstable methods. Instead we transfer volumetric data to each element that has an internal boundary face, we give details below. Given the timestep constraints of DG methods we must march the DG solution using much smaller timesteps than those used for the Hermite method. This necessitates the evaluation of the Hermite data not only at the beginning of a Hermite timestep but at many intermediate times.

4.1 Determining internal boundary data for the Hermite solver

We first consider the problem of determining internal boundary data required by the Hermite method. An example of how to compute solution data at the gridpoints (x_i, y_j) at the boundary of Cartesian grid (filled black circles) is depicted in Figure 1.

In general, the tensor product polynomial centered around (x_i, y_j) is found by a two step procedure. First we project into a local L_2 basis spanned by Legendre polynomials and perform a numerically stable and fast change of basis into the monomial basis. Then we truncate the monomial to the degree required by the Hermite method.

To carry out the L_2 projection we introduce a local tensor product Gauss-Legendre-Lobatto (GLL) grid centered around (x_i, y_j) . These points are marked as filled blue circles in the left subfigure of Figure 2. The number of grid points in the local grids are determined by the order of the projection. To maintain the order of the method, the order of the projection should be at least the same as the order of the spatial discretization, thus it is sufficient to have $2m + 4$ points in each direction. The GLL quadrature nodes are defined on the reference element $(r, s) \in [-1, 1]^2$ that maps to a cell defined by the dual gridpoints closest to (x_i, y_j) .

Let \tilde{u} be the numerical solution on the red grid. In the first step of the communication we compute the coefficients of a polynomial \tilde{p} approximating \tilde{u} by projecting \tilde{u} on the space of tensor product Legendre polynomials $P_l P_k$, that is

$$\tilde{p}(r, s) = \sum_{l=0}^{2m+3} \sum_{k=0}^{2m+3} c_{lk} P_l(r) P_k(s), \quad c_{lk} = \frac{(\tilde{u}, P_l P_k)}{\|P_l P_k\|^2}. \quad (19)$$

Here (f, g) denotes the L_2 inner product on $(r, s) \in [-1, 1]^2$ and $\|f\|_2^2 = (f, f)$ is the norm induced by the inner product. Note that the expression (19) is particularly simple since the Legendre polynomials are orthogonal on the domain of integration. To do this we evaluate \tilde{u} at the underlying blue quadrature points in the left subfigure of Figure 2.

Once the polynomial (19) has been found we perform a change of basis into the local monomial used by the Hermite method. Such a change of basis can be done by the fast Vandermonde techniques by Björk and Pereyra, see e.g. [10, 17]. At this stage the polynomial is of total degree $2m + 3$ so the final step is to truncate it to total degree m or $m + 1$ depending on whether we are considering the displacement

or the velocity. With the $(m+1)^2$ and $(m+2)^2$ degrees of freedom determined everywhere on a Hermite grid we may evolve the solution as described in section 2.

4.2 Determining data for DG elements with internal boundary faces

We now consider the problem of determining the data required by the DG method. Here we show how to obtain the data at a single DG element with at least one internal boundary face. As the timesteps of the DG method are significantly smaller than for the Hermite method we must repeat the transfer of data many times. We must also explicitly transfer time derivative data in order to use a Taylor series timestepping approach.

The tensor product polynomials in our implementation of the DG method are composed by the product of Chebyshev polynomials $T_j(z) = \cos(j \cos^{-1}(z))$ that are expressed on the reference element $(r, s) \in [-1, 1]^2$. Precisely we seek

$$p(r, s) = \sum_{l=0}^q \sum_{k=0}^q c_{lk} T_l(r) T_k(s).$$

To determine such polynomials we perform a projection of the solution u , i.e the solution on Cartesian grid,

$$c_{lk} = \frac{(\tilde{u}, T_l T_k)_C}{\|T_l T_k\|_C^2},$$

but in this case the weighted inner product is

$$(f, g)_C = \int_{-1}^1 \int_{-1}^1 \frac{f(r, s) g(r, s)}{\sqrt{1-r^2} \sqrt{1-s^2}} dr ds,$$

where the Chebyshev polynomials are orthogonal. To carry out this projection we use a local tensor product Chebyshev quadrature nodes, $2m+2$ in each dimension, as shown in right subfigure of Figure 2.

Denoting The local time levels used by the DG solver n th Hermite timestep are defined to be

$$t_{n,\nu} = t_{n,0} + \nu \Delta t_b, \quad \nu = 0, \dots, N_{\text{DG}},$$

where Δt_a and Δt_b are timesteps taken on grids a (Cartesian) and b (curvilinear) respectively. For simplicity the starting local time level and the final local time level are equal to consequent timesteps on the Hermite grid, t_n and t_{n+1}

$$t_{n,0} = t_n, \quad t_{n,N_{\text{DG}}} = t_{n+1}.$$

To transfer the solution values and the time derivatives needed at each of the quadrature points and at each $t_{n,\nu}$ we carry out the following “start up” procedure at $t_{n,0}$. For each of the quadrature points we re-center the Hermite interpolants closest to it and compute the time derivatives precisely by the recursion relations described in section 2. We note that this is an inexpensive computation as the interpolants have already been found as a step in the evolution of the Hermite solution, the only added operation is the re-centering.

5 Numerical experiments

The hybrid H–DG method is empirically stable and accurate, and here we demonstrate it with numerical experiments. To test the stability of the method in one dimension we first define the amplification matrix and compute its spectral radius. To test the stability in two dimensions, where the amplification matrix will take too long to compute, we provide the long time simulation and estimate the error growth for multiple refinements. Convergence tests in one and two dimensions are done for the domains where the exact solution is known. In the second half of this section we apply the method to the domain with complex curvilinear boundary in the experiment with wave scattering of the smooth pentagonal object. Finally, in the end of this section we apply the method to the inverse problem of locating the underground cavities as the forward solver.

5.1 Numerical stability test

Unlike the Hermite and DG methods, stability of the hybrid H–DG method cannot be shown analytically. As an alternative, the stability can be investigated numerically by looking at the spectrum of the amplification matrix associated with the method. A similar stability analysis was done for finite difference scheme for the wave equation in [32]. To construct the amplification matrix we apply the method to initial data composed of the unit vectors. The vector that is returned after one timestep is then placed as columns in a square matrix. The spectral radius of the amplification has to be smaller than 1 for the method to be stable.

We consider the wave equation (1)–(2) on the unit interval $x \in [0, 1]$ with homogeneous Dirichlet and Neumann boundary conditions at $x = 0$ and $x = 1$ respectively. We introduce two uniform Cartesian grids which overlap inside a small interval close to one of the boundaries. Precisely, the grids are

$$\begin{aligned}\Omega_a &= \{x_i^a = ih_a, \quad i = 0, \dots, n_a\}, \\ \Omega_b &= \{x_i^b = 1 - (n_b - i)h_b, \quad i = 0, \dots, n_b\}.\end{aligned}$$

The Hermite method is used on a grid a and the DG method is used on grid b . The grids thus overlap inside the interval $[x_0^b, x_{n_a}^a]$. Here the ratio of the overlap size and the discretization width is $(x_{n_a}^a - x_0^b)/h_a$. This ratio is fixed for all values of h_a and h_b . We also fix n_b so that the amount of work done on grid b is constant per timestep for all refinements. Fixing the ratio $(x_{n_a}^a - x_0^b)/h_a$ and n_b makes the efficiency of the overall method to asymptotically be determined by the efficiency of the Hermite method.

Let \mathbf{w}^n be a vector holding the degrees of freedom of both methods at n th timestep, then we may express the complete timestep evolution as $\mathbf{w}^{n+1} = \mathcal{H}\mathbf{w}^n$ where \mathcal{H} incorporates timestepping and projection. \mathcal{H} can be expressed as the matrix H that can be computed column by column via

$$H_k = \mathcal{H}e_k, \tag{20}$$

where e_k is the k th unit vector. The equation

$$\mathbf{w}^n = H^n \mathbf{w}^0, \tag{21}$$

is equivalent to the n timesteps of the hybrid H-DG method. Taking 2-norm of both sides of equation (21) and applying the Cauchy-Schwartz inequality we get

$$\|\mathbf{w}^n\|_2 \leq \|H\|_2^n \|\mathbf{w}^0\|_2 \leq \lambda^n \|\mathbf{w}^0\|_2,$$

where $\lambda = \rho(H)$ is the spectral radius of H . If $\lambda \leq 1$ we conclude

$$\|\mathbf{w}^n\|_2 \leq \|\mathbf{w}^0\|_2,$$

and the solution will remain bounded.

We consider the case $c = 1$ and take the parameters to be

$$n_a = 10, 20, \dots, 60, \quad n_b = 5, \quad \frac{h_b}{h_a} = 0.9.$$

Other parameters are q_u, q_v for the DG method and n_{DG} , the number of timesteps done by the DG method during one step of the Hermite method. The parameters q_u and q_v are set so the methods used have the same order of accuracy as the approximation of v for the Hermite method

$$q_u = 2m + 2, \quad q_v = 2m + 1.$$

To get an optimal n_{DG} , we take the largest possible timestep for the DG method, so that

$$\frac{\Delta t_b}{h_b} \leq 0.15/q_u,$$

and

$$n_{DG} = \frac{\Delta t_a}{\Delta t_b},$$

is an integer. Equivalently, if the Hermite method CFL number is set, we get

$$n_{DG} = \frac{\Delta t_a}{\Delta t_b} = \left\lceil \text{CFL} \frac{q_u}{0.15} \frac{h_a}{h_b} \right\rceil.$$

Following the column-by-column construction process (20) described at the start of this section we compute the amplification matrix H for the current setting. The spectrum of H is shown in Figure 3 for $m = 1, 2, 3$. Displayed results are for the cases $n_a = 40$ and $n_b = 5$. The CFL numbers set for Hermite method are $\Delta t_a/h_a = 0.5$ and 0.8 . The absolute value of eigenvalues do not exceed 1. We note that if interpolation is used some eigenvalues of the amplification matrix shift outside of the unit circle. Such unstable modes can possibly be stabilized by numerical dissipation / hyperviscosity but we do not pursue such stabilization here. Instead we observe that when projection is used all eigenvalues are inside the unit circle and the method is stable. Although we only display the results for one problem here the same results were obtained for other grid sizes, various overlap sizes to grid spacing ratios and different CFL numbers set for the Hermite method. We stress that it is possible to make the method unstable if we take the CFL number close to one and if we take m to be larger than 3 and thus we only claim that the methods of orders of accuracy up to 7 are stable.

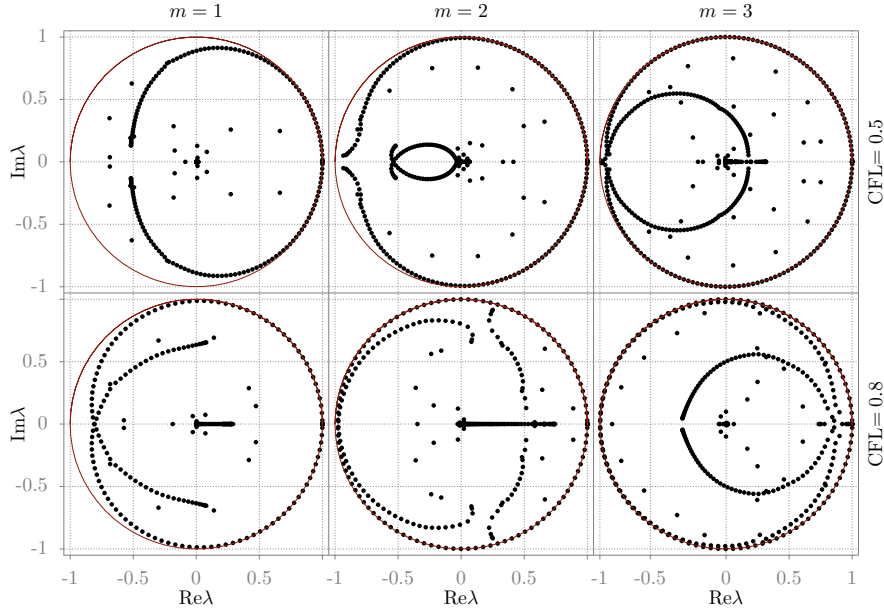


Fig. 3 Spectrum of the amplification matrix H for CFL numbers $\Delta t_a/h_a = 0.5, 0.8$, orders of accuracy 3, 5, 7, and $n_a = 40$, $n_b = 5$. No eigenvalues are outside the unit circle.

5.2 Convergence to an exact solution

Using the same grid setup and boundary conditions as in the example above we test the method for the wave equation (1)-(2), $c = 1$ and initial conditions

$$u(x, 0) = \sin\left(\frac{15\pi}{2}x\right), \quad (22)$$

$$v(x, 0) = 0. \quad (23)$$

A solution to this problem is the standing wave

$$u(x, t) = \sin\left(\frac{15\pi}{2}x\right) \cos\left(\frac{15\pi}{2}t\right).$$

The errors for the solution on the grids are

$$\varepsilon_a(x, t) = p_{i+\frac{1}{2}}(x, t) - u(x, t), x \in x_i^a, x_i^a + 1, i = 0, \dots, n_a, \quad (24)$$

for the Hermite grid and

$$\varepsilon_b(x, t) = u^{h_b}(x, t) - u(x, t), \quad (25)$$

for the DG grid. The maximum error for the total method is

$$\max\left(\max_{x \in [x_0^a, x_{n_a}^a]} |\varepsilon_a(x, t)|, \max_{x \in [x_0^b, x_{n_b}^b]} |\varepsilon_b(x, t)|\right).$$

In Figure 4 we display computed maximum errors as functions of time for the method with $m = 3$ (i.e. the order of accuracy is 7). In the left subfigure the CFL number for the Hermite method is set to be 0.5 and in the right subfigure the CFL number is set to be 0.75. For all Hermite grid sizes, the error growth is linear in time (dashed lines display a least squares fit of a linear function), indicating that the solution is stable for long time computations.

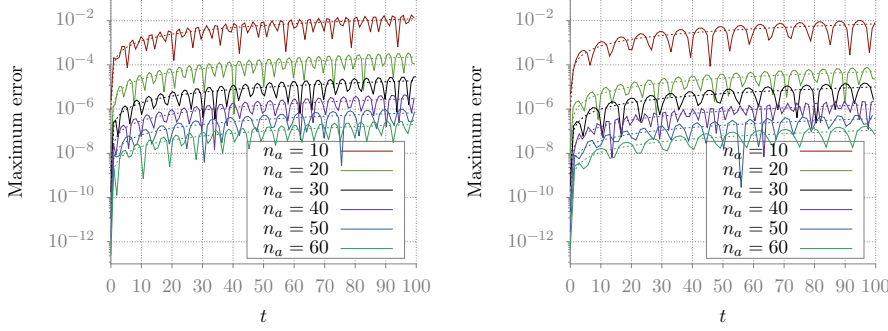


Fig. 4 Maximum error of the solution as a function of time. The curves correspond to different refinements for $m = 3$. In the left subfigure CFL number for Hermite method is set to 0.5. In the right subfigure CFL number for Hermite method is set to 0.75. Dashed lines display lines αt .

In the left subfigure of Figure 5 the numerical solution and the absolute error are shown for the 7th order accurate method at time $t = 2$. As can be seen in the lower left subfigure in Figure 5 the error is rather smooth across the overlap indicating that the projection is highly accurate.

To the right in Figure 5 the error at the final time $t = 2$ is shown as a function $h = h_a$. The dashed lines show the least squares fit with polynomial functions of h_a of order 3, 5 and 7 respectively. The results indicate that the orders of accuracy of the methods are $2m + 1$ as expected. The parameters (n_a , n_b , n_{DG} , etc.) are the same as in previous example.

5.3 Analytical solution in a disk. Rates of convergence

Consider the solution of (1)-(2) with $f(x, y, t) \equiv 0$ on the unit disk, $(x, y) \in x^2 + y^2 \leq 1$, with homogeneous Dirichlet boundary conditions. Then the analytical solution can be expressed in polar coordinates as a composition of modes

$$u_{\mu\nu}(r, \theta, t) = J_\mu(r\kappa_{\mu\nu}) \cos(\mu\theta) \cos \kappa_{\mu\nu} t. \quad (26)$$

Here $J_\mu(z)$ is the Bessel function of the first kind of order μ and $\kappa_{\mu\nu}$ is the ν th zero of J_μ . In the following experiment we set $\mu = \nu = 7$, $\kappa_{77} = 31.4227941922$. The initial condition $u_{77}(x, y, 0)$ is displayed in the left subfigure of Figure 6.

We setup overset grids as displayed in Figure 7. Grid a is a Cartesian grid discretizing a square domain with $2n_a + 1$ grid points in each direction and grid

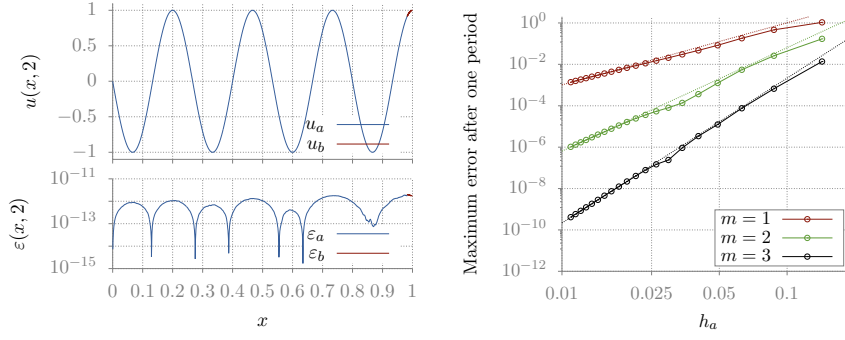


Fig. 5 The upper left subfigure displays the solution at time $t = 2$. The error at time $t = 2$ is shown in the lower left subfigure. The number of grid points are $n_a = 200$, $n_b = 5$ and $m = 3$, the Hermite CFL number is set to 0.75. Red curves indicate the solution and the error on the DG grid. Blue curves indicate the solution and the error on the Hermite grid. (The solution and the error were computed on finer grid, 10 grid points per cell/element). In the right subfigure we display a convergence plot for $m = 1, 2, 3$. Dashed lines show the least squares fit of $C_m h_a^q$, $q = 3, 5, 7$.

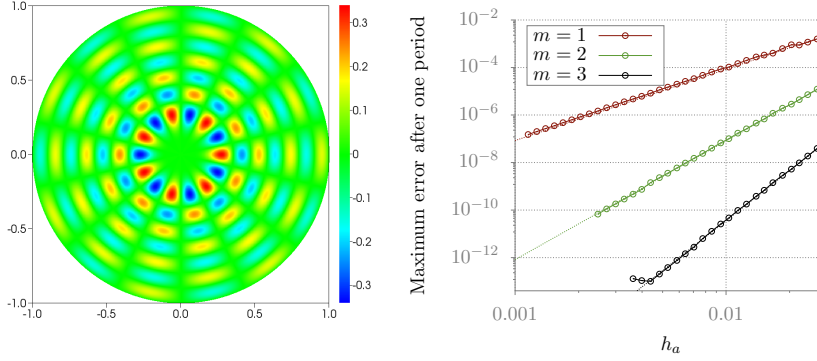


Fig. 6 The left subfigure displays the initial condition. In the right subfigure the max-error at time $t = 2\pi/\kappa_{77}$ as a function of grid spacing of the Hermite method. Solid curves correspond to the methods with $m = 1, 2, 3$ and dashed lines display the expected convergence rates i.e. $\mathcal{O}(h_a^{2m+1})$.

spacing $h_a = 1/n_a$. Grid b is a curvilinear grid discretizing a thin annulus with radial grid spacing $1.1h_a$. For all refinements Grid b has 7 elements in the radial direction thus the number of elements (or equivalently the number of DOFs of DG method) will grow linearly with the reciprocal of the discretization size h_a . In contrast the number of grid points in the Cartesian grid where the Hermite method will be used grows quadratically with $1/h_a$.

To measure the error we evaluate the solution on a finer grid, oversampled with 20 grid points inside each Hermite cell and DG element. The convergence is displayed in the right subfigure of Figure 6. The errors at time $t = 2\pi/\kappa_{77}$ as functions of h_a for $m = 1, 2, 3$ are displayed as solid lines. The dashed lines show the polynomials in h_a of order $2m + 1$. We use $h_a = 1/34, 1/36, \dots, 1/94$ in the

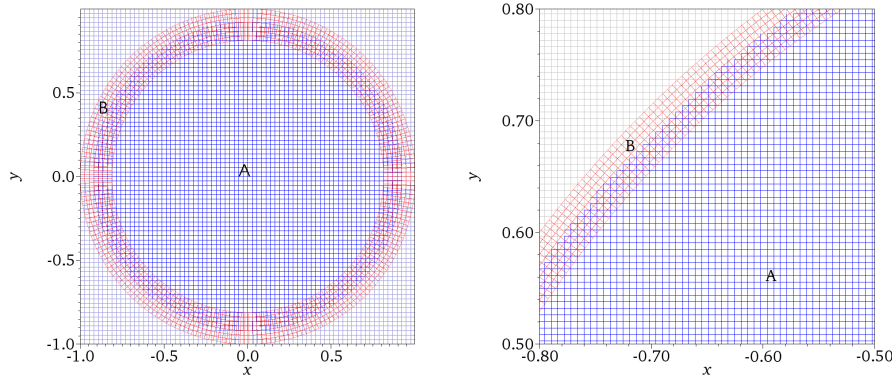


Fig. 7 Overset grid set up for two different discretization widths. The Hermite grid is blue and DG grid is red. The Hermite grid is truncated at radius $1 - h_a$, i.e one Hermite grid spacing smaller than the computational domain. This creates a stair shaped interior boundary. The solution at that boundary is imposed by the projection described above. The curvilinear grid has 7 elements in the radial direction, thus the number of elements grows linearly with n_a . The number of grid points in the Hermite grid grows as n_a^2 .

computations. As can be seen the expected orders of accuracy (3,5 and 7) are observed.

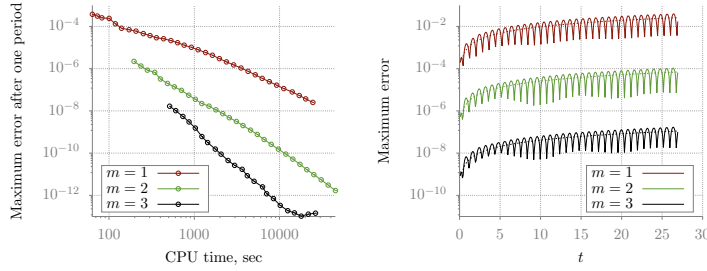


Fig. 8 In the left subfigure the error at fixed time $t = 2\pi/\kappa_{77}$ is shown as a function of CPU time. The right subfigure displays the error as a function of time t . Dashed lines are the linear functions αt formed by a least squares fit.

To test the performance of the method we evolve the method over one time period of the solution and measure the CPU time, see the left subfigure of Figure 8. The red curve, displaying the error of the 3rd, order accurate method only reaches the error 10^{-6} in about 1000 seconds while the 5th and 7th order accurate methods, using the same compute time, yield errors on the order of 10^{-8} and 10^{-10} respectively. Clearly the higher order methods are more efficient.

To test the stability of the method we evolve the solution until time $t = 60\pi/7$ which is roughly 130 periods of the solution. We set $h_a = 1/54$ and test methods with orders of accuracy 3, 5 and 7. The error growth appears to be linear in time as indicated by dashed lines in the right subfigure of Figure 8.

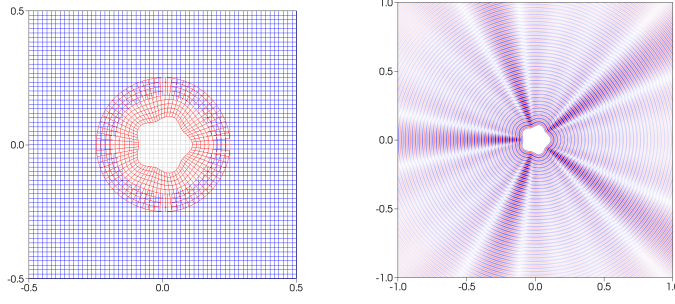


Fig. 9 Left: Overset grid set up around the body. The overlapping DG grid and background Cartesian grid shown on the domain $[-0.5, 0.5]^2$. Right: Snapshot of $u(x, y, 10)$.

5.4 A wave scattering of a smooth pentagon

In this experiment we study the scattering of a smooth pentagon in free-space. In addition to the use of non-reflecting boundary conditions experiment demonstrates the hybrid Hermite-DG method for the solution which is propagated over many wavelengths. The geometry of the pentagon is defined as the smooth closed parametric curve:

$$x(s) = \frac{1}{10} \left(1 + \frac{1}{10} \cos(10s) \right) \cos(s), \quad (27)$$

$$y(s) = \frac{1}{10} \left(1 + \frac{1}{10} \cos(10s) \right) \sin(s), \quad s \in [0, 2\pi). \quad (28)$$

The pentagon is placed in a square domain $(x, y) \in [-2, 2]^2$ discretized by a Cartesian grid with grid spacing $1/n$, $n = 40$. The curvilinear grid has 10 elements in the radial direction and the outer boundary is a circle of radius $0.1 + 20/n$. The overlap width is at most 5 DG elements.

On the boundary of the body we set Dirichlet data

$$u(x, y, t) = \sin(\omega t), \quad (x, y) \in \Gamma, \quad t \geq 0, \quad \omega = 250. \quad (29)$$

The exterior boundary condition is modeled by truncating the domain using perfectly matched layers governed by the equations, (see [6] for derivation)

$$u_{tt} = \frac{\partial}{\partial x} \left(u_x + \sigma^x \phi^{(1)} \right) + \frac{\partial}{\partial y} \left(u_y + \sigma^y \phi^{(2)} \right) \sigma^{(x)} \phi^{(3)} + \sigma^{(y)} \phi^{(4)}, \quad (30)$$

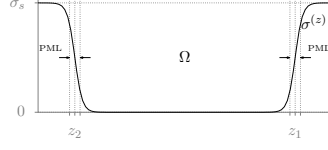


Fig. 10 The damping profile $\sigma^{(z)}$ for PML with damping strength σ_s . The damping is zero at the center of the domain Ω and rapidly increases in the PML on the both edges of the domain.

where the auxiliary variables satisfy the equations

$$\begin{aligned}
 \phi_t^{(1)} + (\alpha + \sigma(x))\phi^{(1)} &= -u_x, \\
 \phi_t^{(2)} + (\alpha + \sigma(y))\phi^{(2)} &= -u_y, \\
 \phi_t^{(3)} + (\alpha + \sigma(x))\phi^{(3)} &= -u_{xx} - \frac{\partial}{\partial x} \left(\sigma^{(x)} \phi^{(1)} \right), \\
 \phi_t^{(4)} + (\alpha + \sigma(y))\phi^{(4)} &= -u_{yy} - \frac{\partial}{\partial y} \left(\sigma^{(y)} \phi^{(2)} \right).
 \end{aligned} \tag{31}$$

The damping profiles $\sigma^{(z)}$, $z = x, y$ are taken as

$$\sigma^{(z)}(z) = \sigma_s \left(\tanh \left(\frac{z - z_1}{0.7w_{\text{lay}}} \right) - \tanh \left(\frac{z - z_2}{0.7w_{\text{lay}}} \right) \right).$$

Here σ_s is a damping strength, w_{lay} is layer width and z_1 and z_2 control the location of the damping profile of the PML. The shape of $\sigma^{(z)}$ is displayed in Figure 10.

Remark 3 In experiments involving PML we discretize the modified equations (30) only with Hermite method. It is straightforward to construct the computational domain with PML so that the DG mesh lie inside the computational domain.

The order of accuracy of the methods is set to be 7, i.e. $q_u = q_v = 6$, and $m = 3$. The solution is evolved to $t = 10$. A snapshot of the solution at the final time is displayed in the right subfigure of Figure 9. The proposed algorithm clearly is able to accurately propagate waves in complex domains.

5.5 Wave scattering of many cylinders in free space

As another demonstration of the method we simulate a domain with multiple circular holes. Precisely we consider the infinite domain $\Omega \in [-\infty, \infty] \times [-\infty, 1.33]$ with homogeneous Neumann boundary condition at $y = 1.33$. The computational domain is a rectangle $[-1, 1] \times [-1.33]$ with PML $|x| > 1$ and $y < -1$. Inside the computational domain there are 5 cylinders of radii 0.1 and centers at (x_k, y_k) , $k = 1, \dots, 5$. We impose the homogeneous Dirichlet boundary conditions

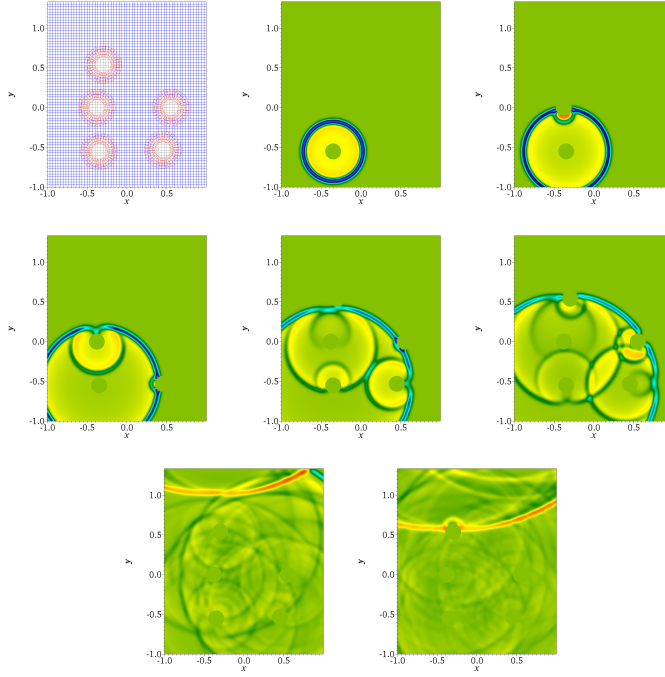


Fig. 11 Overset grid setup and solution plots for 5 bodies in a free half space. In the upper left subfigure the grids are shown: DG gridlines plotted with red color, Cartesian grid lines inside the domain plotted with blue. Other figures are the solution plots at various increasing times.

on the boundary of all cylinders except first. On the first cylinder we impose a time dependent boundary condition

$$u(t, x, y) = (t - 0.1) \exp\left(-918(t - 0.1)^2\right), \quad (x, y) \in \{(x - x_1)^2 + (y - y_1)^2 = 0.01\}.$$

The initial solution is at rest.

The set up of the numerical method is similar to the previous experiment. The Cartesian grid covers the background domain and the PML. The 5 circular grids are placed around the bodies as shown in the upper left subfigure Figure 11. In this experiment we used the 7th order method. It can be noticed that as in all solution plots provided in this paper the solution is smooth across the overlap due to the high accuracy of methods used and the projection used for communication.

5.6 An inverse problem, locating a body in free space

As a final experiment we solve the inverse problem of locating a cylindrical body in free space. An application of this problem could be a to locate a tunnel under the ground and determining its radius by sending waves from source devices buried at a relatively small distance from the surface and recording the solution near

the surface. Waves will propagate from a source, reflect from an underground cavity and travel back to the surface to be captured by the recording devices. The underground cavity can be located by minimizing a cost functional, i.e misfit function of recorded data and data obtained from the numerical simulation in each iteration of the optimization process.

Consider a square region $\Omega \in [-1, 1] \times [-1, 1.25]$ with 3 circular bodies of radius $r = 0.1$ with centers at $x_1 = -0.7$, $x_2 = 0$, $x_3 = 0.7$ and $y_1 = y_2 = y_3 = -0.7$. On the boundary of the bodies we impose homogeneous Dirichlet boundary conditions. On the top boundary $y = 1.33$, that acts as a "ground surface" we impose homogeneous Neumann boundary conditions. The exterior boundary conditions at $x = \pm 1$ and $y = -1$ are imposed by truncating the domain using PML. We discretize the domain with a Cartesian grid. Around each of the cavities we place annular DG grids that are 5 cell wide. An example of a complete set up with 4 receivers is shown in Figure 12.

First we create synthetic data by recording the displacement u at equidistant locations of the receivers

$$(0, 0.125), (0.25, 0.125), (0.25, 0.125), (0.25, 0.125),$$

to time $T = 2$. Let there be another circular body of radius A_1 and center at $(x, y) = (A_2, A_3)$ we want to locate. In the right figure the first source is active, i.e. the initial condition is a smooth Gaussian centered at $\hat{x} = -0.25$, $\hat{y} = 1$, with no initial velocity

$$u(0, x, y) = \exp\left(-40\left((x - \hat{x})^2 + (y - \hat{y})^2\right)\right), \quad v(0, x, y) \equiv 0. \quad (32)$$

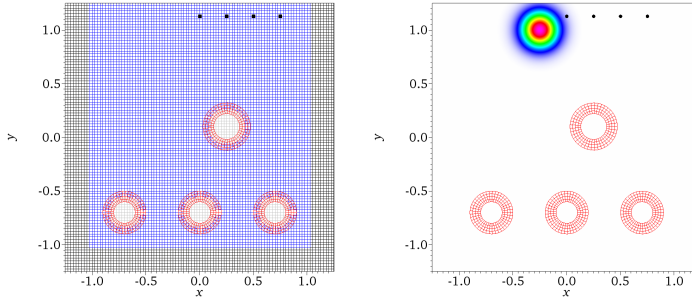


Fig. 12 The inverse problem set up. Receivers are marked as dots. The left subfigure displays the complete overset grid set up, with 4 DG grids around bodies, and a Cartesian background grid. Blue and red grids discretize physical subdomain; the black grid is the PML layer; the gray grids indicate the subdomains covered by DG grids. The right subfigure displays of the initial condition, a smooth Gaussian centered at $(-0.25, 1)$, receivers and the DG grids.

First we create the synthetic data for the exact location of the target, $A_1^* = 0.12$, $A_2^* = 0.25$ and $A_3^* = 0.1$. This gives us u^* . To locate the cavity we minimize

N iter.	A_1	A_2	A_3	F	$\ \nabla F\ $
0	$1.0100E-01$	$2.5250E-01$	$1.2120E-01$	$7.83582E-06$	$4.41312E-03$
1	$1.0117E-01$	$2.5077E-01$	$1.1944E-01$	$1.96547E-07$	$2.88478E-04$
2	$1.0117E-01$	$2.5066E-01$	$1.1955E-01$	$1.38952E-07$	$2.32250E-04$
3	$1.0105E-01$	$2.5012E-01$	$1.2000E-01$	$2.26171E-08$	$4.32507E-05$
4	$1.0095E-01$	$2.5010E-01$	$1.2001E-01$	$1.87633E-08$	$3.97138E-05$
5	$1.0002E-01$	$2.4999E-01$	$1.2001E-01$	$5.81672E-11$	$5.80355E-06$
6	$1.0000E-01$	$2.5000E-01$	$1.2000E-01$	$1.00121E-15$	$4.21271E-08$

Table 1 Convergence results of L-FBGS-B algorithm for the inverse problem for locating a body in free space. At each iteration the cost function F and its gradient ∇F is computed from the numerical solution of the wave equation. The forward solver is implemented using the 5th order accurate Hybrid Hermite-DG overset grid method.

the cost function that is a sum of squared L_2 norms of discrepancies between the output of the numerical simulation and synthetic data $u^*(t, \tilde{x}_l, 0.125)$

$$F(A_1, A_2, A_3) = \sum_{l=1}^4 \int_0^T (u(t, \tilde{x}_l, 0.125) - u^*(t, \tilde{x}_l, 0.125))^2. \quad (33)$$

During the minimization we impose the bounds $0.01 \leq A_1 \leq 0.2$, $|A_2| < 0.5$, $|A_3| < 0.2$. To recover A_1^*, A_2^* we use the L-BFGS-B algorithm, (see [12] for description). Forward differences are used to compute the gradients, resulting in total $1 + 3$ simulations per iteration. Table 1 displays the convergence results in detail for the initial values 0.101, 0.2525 and 0.1212. At the 6th iteration the values computed were 0.1, 0.25 and 0.12, accurate to the 8th digit.

6 Summary

We have presented overset high order numerical methods for numerical solution of the wave equation. The hybrid H-DG overset grid method combines the highly efficient Hermite method on Cartesian grids with a DG method to treat complex boundaries. To combine the methods the overset grids were used. The advantage of using the overset grids for complex boundary problems is the low computational cost that asymptotically approaches the cost of the Cartesian solver.

In this work we communicate solutions via L_2 projection and this procedure combined with the dissipative nature of the methods was observed to be sufficient to guarantee stability without the need to add any artificial dissipation.

Stability, accuracy and efficiency of the method were tested numerically. To test the stability in 1 dimension, we looked at the spectrum of the amplification matrix associated with the method. For CFL numbers < 0.75 for the Hermite method, the overall method was stable in all tested settings for grid sizes and orders of accuracy 3, 5 and 7. In 1 and 2 dimensions we also tested the stability by displaying the error growth as a function of time for long times.

Finally, three example applications of the methods were presented. First, the wave scattering of the pentagonal object in free space was shown, demonstrating the use of the method for the problem with curvilinear boundary and free space boundary conditions. Second, a simulation with five round objects in free space

was demonstrated. Finally the method was used to solve the inverse problem of locating a cylindrical underground body.

A future extension could be to improve the efficiency of the DG method used on the curvilinear body fitted grids by the use of an implicit timestepping method. This would allow the timesteps to be commensurate to those of the Hermite method at a relatively low cost since the linear systems needed to be inverted would be essentially one dimensional. Another natural extension of this work would be to apply the techniques presented here to the elastic wave equation.

Acknowledgements This work was supported in part by the National Science Foundation under Grant NSF-1913076. Any opinions, findings, and conclusions or recommendations expressed in this material are those of the author(s) and do not necessarily reflect the views of the National Science Foundation.

Conflict of interest

The authors declare that they have no conflict of interest.

References

1. Angel, J.B., Banks, J.W., Henshaw, W.D.: High-order upwind schemes for the wave equation on overlapping grids: Maxwell's equations in second-order form. *Journal of Computational Physics* **352**, 534 – 567 (2018)
2. Appelö, D., Banks, J.W., Henshaw, W.D., Schwendeman, D.W.: Numerical methods for solid mechanics on overlapping grids: Linear elasticity. *Journal of Computational Physics* **231**(18), 6012–6050 (2012)
3. Appelö, D., Hagstrom, T.: A new discontinuous Galerkin formulation for wave equations in second order form. *SIAM Journal On Numerical Analysis* **53**(6), 2705–2726 (2015)
4. Appelö, D., Hagstrom, T.: An energy-based discontinuous Galerkin discretization of the elastic wave equation in second order form. *Computer Methods in Applied Mechanics and Engineering* **338**, 362–391 (2018)
5. Appelö, D., Hagstrom, T., Vargas, A.: Hermite methods for the scalar wave equation. *SIAM Journal on Scientific Computing* **40**(6), A3902–A3927 (2018)
6. Appelö, D., Petersson, N.: A fourth-order accurate embedded boundary method for the wave equation. *SIAM Journal on Scientific Computing* **34**(6), A2982–A3008 (2012)
7. Appelö, D., Wang, S.: An energy based discontinuous Galerkin method for coupled elasto-acoustic wave equations in second order form. Published to *International Journal for Numerical Methods in Engineering* 2018
8. Banks, J.W., Hagstrom, T.: On galerkin difference methods. *Journal of Computational Physics* **313**, 310 – 327 (2016)
9. Banks, J.W., Henshaw, W.D.: Upwind schemes for the wave equation in second-order form. *Journal of Computational Physics* **231**(17), 5854 – 5889 (2012)
10. Björck, Å., Pereyra, V.: Solution of Vandermonde systems of equations. *Mathematics of Computation* **24**(112), 893–903 (1970)
11. Bruno, O.P., Lyon, M.: High-order unconditionally stable FC-AD solvers for general smooth domains I. Basic elements. *Journal of Computational Physics* **229**(6), 2009 – 2033 (2010)
12. Byrd, R.H., Lu, P., Nocedal, J., Zhu, C.: A limited memory algorithm for bound constrained optimization. *SIAM Journal on Scientific Computing* **16**(5), 1190–1208 (1995)
13. Chesshire, G., Henshaw, W.D.: Composite overlapping meshes for the solution of partial differential equations. *Journal of Computational Physics* **90**(1), 1–64 (1990)
14. Chou, C.S., Shu, C.W., Xing, Y.: Optimal energy conserving local discontinuous Galerkin methods for second-order wave equation in heterogeneous media. *Journal of Computational Physics* **272**, 88 – 107 (2014)

15. Chung, E.T., Engquist, B.: Optimal discontinuous Galerkin methods for wave propagation. *SIAM Journal on Numerical Analysis* **44**(5), 2131–2158 (2006)
16. Chung, E.T., Engquist, B.: Optimal discontinuous Galerkin methods for the acoustic wave equation in higher dimensions. *SIAM Journal on Numerical Analysis* **47**(5), 3820–3848 (2009)
17. Dahlquist, G., Björck, Å.: *Numerical methods in scientific computing*. Society for Industrial and Applied Mathematics (2008)
18. Goodrich, J., Hagstrom, T., Lorenz, J.: Hermite methods for hyperbolic initial-boundary value problems. *Mathematics of computation* **75**(254), 595–630 (2006)
19. Grote, M.J., Schneebeli, A., Schötzau, D.: Discontinuous Galerkin finite element method for the wave equation. *SIAM Journal on Numerical Analysis* **44**(6), 2408–2431 (2006)
20. Hagstrom, T., Appelö, D.: Solving PDEs with Hermite interpolation. In: *Spectral and High Order Methods for Partial Differential Equations ICOSAHOM 2014*, pp. 31–49. Springer (2015)
21. Hagstrom, T., Hagstrom, G.: Grid stabilization of high-order one-sided differencing II: Second-order wave equations. *Journal of Computational Physics* **231**(23), 7907 – 7931 (2012)
22. Henshaw, W.D.: Ogen: An overlapping grid generator for Overture. Research Report UCRL-MA-132237, Lawrence Livermore National Laboratory (1998)
23. Henshaw, W.D.: A high-order accurate parallel solver for Maxwell’s equations on overlapping grids. *SIAM Journal on Scientific Computing* **28**(5), 1730–1765 (2006)
24. Li, J.R., Greengard, L.: High order marching schemes for the wave equation in complex geometry. *Journal of Computational Physics* **198**(1), 295 – 309 (2004)
25. Lyon, M., Bruno, O.P.: High-order unconditionally stable FC-AD solvers for general smooth domains II. Elliptic, parabolic and hyperbolic PDEs; theoretical considerations. *Journal of Computational Physics* **229**(9), 3358 – 3381 (2010)
26. Mattsson, K., Nordström, J.: Summation by parts operators for finite difference approximations of second derivatives. *Journal of Computational Physics* **199**, 503–540 (2004)
27. Nguyen, N.C., Peraire, J., Cockburn, B.: High-order implicit hybridizable discontinuous Galerkin methods for acoustics and elastodynamics. *Journal of Computational Physics* **230**(10), 3695 – 3718 (2011)
28. Petersson, N.A., Sjögreen, B.: High order accurate finite difference modeling of seismo-acoustic wave propagation in a moving atmosphere and a heterogeneous earth model coupled across a realistic topography. *Journal of Scientific Computing* **74**(1), 290–323 (2018)
29. Stanglmeier, M., Nguyen, N.C., Peraire, J., Cockburn, B.: An explicit hybridizable discontinuous Galerkin method for the acoustic wave equation. *Computer Methods in Applied Mechanics and Engineering* **300**, 748 – 769 (2016)
30. Sticko, S., Kreiss, G.: Higher order cut finite elements for the wave equation. arXiv preprint arXiv:1608.03107 (2016)
31. Sticko, S., Kreiss, G.: A stabilized Nitsche cut element method for the wave equation. *Computer Methods in Applied Mechanics and Engineering* **309**, 364 – 387 (2016)
32. Strikwerda, J.C.: *Finite difference schemes and partial differential equations*, vol. 88. SIAM (2004)
33. Virta, K., Mattsson, K.: Acoustic wave propagation in complicated geometries and heterogeneous media. *Journal of Scientific Computing* **61**(1), 90–118 (2014)
34. Wandzura, S.: Stable, high-order discretization for evolution of the wave equation in 2 + 1 dimensions. *Journal of Computational Physics* **199**(2), 763 – 775 (2004)
35. Wang, S., Virta, K., Kreiss, G.: High order finite difference methods for the wave equation with non-conforming grid interfaces. *Journal of Scientific Computing* **68**(3), 1002–1028 (2016)
36. Wilcox, L., Stadler, G., Burstedde, C., Ghattas, O.: A high-order discontinuous Galerkin method for wave propagation through coupled elastic-acoustic media. *Journal of Computational Physics* **229**(24), 9373–9396 (2010)